*Q. J. R. Meteorol. Soc.* (2005), **131**, pp. 3079–3102 doi: 10.1256/qj.04.106

# A kinetic energy backscatter algorithm for use in ensemble prediction systems

By GLENN SHUTTS*
*European Centre for Medium-Range Weather Forecasts, Reading, UK*

(Received 15 July 2004, revised 20 June 2005)

SUMMARY

Physical justification is provided for the use of kinetic energy backscatter in forecast models, particularly in respect of ensemble prediction systems. The rate of energy backscatter to scales near the truncation limit is controlled by a total energy dissipation function involving contributions from numerical diffusion, mountain drag and deep convection. A cellular automaton is used to generate evolving patterns that, together with the dissipation function, define a stream-function forcing field. Each member of the European Centre for Medium-Range Weather Forecasts (ECMWF) ensemble forecast system is perturbed by a different realization of this backscatter forcing, and the resulting increase in ensemble spread, if not excessive, has a beneficial impact on probabilistic measures of forecast skill. The input of small-scale kinetic energy by the backscatter algorithm also helps to correct a known problem with the energy spectrum in the ECMWF model—the absence of the observed $-5/3$ spectral slope in the mesoscales.

KEYWORDS: Cellular automaton Dissipation Stochastic

## 1. INTRODUCTION

Forecast error is deemed to be the result of imperfections both in the initial atmospheric state and in numerical weather forecast model formulation. Model error is associated with basic design choices that define the adiabatic framework of the model (e.g. spectral, grid point, finite element; vertical coordinate system; the advection scheme and its related truncation error) and a component due to errors in physical parametrization. Ensemble prediction systems exploit the sensitivity of numerical weather forecasts to initial conditions and carry out many forecasts from slightly different initial atmospheric states. In order to address forecast error resulting from model imperfections, the European Centre for Medium-Range Weather Forecasts (ECMWF) Ensemble Prediction System (EPS) attempts to account for the uncertainty in parametrized fluxes associated with the statistical nature of the subgrid-scale processes they represent (Buizza *et al.* 1999). In this approach the subgrid-scale parametrization tendency at all points within predefined latitude/longitude boxes is multiplied by a number selected randomly, with uniform probability, from the range 0.5 to 1.5. Each physical parametrization scheme has its own set of random numbers to perturb it. A uniform latitude/longitude grid with 10-degree resolution is used operationally to define the boxes and the random numbers are updated every 6 h.

The random numbers used in the ECMWF EPS have crude spatial and temporal correlation through their constancy within the boxes and within 6 h time intervals. In middle latitudes this spatial correlation-scale is comparable with the Rossby deformation radius and the time-scale is about twice the Coriolis time-scale ($1/f$, where $f$ is the Coriolis parameter) implying that the resulting flow perturbations will project well onto the balanced part of the flow. Smaller correlation-scales tend to generate high-frequency gravity waves whose impact on weather system evolution is only slight. Perturbations in the parametrization increments generated by the scheme are meant to represent statistical fluctuations about the ensemble-mean value. In the case of convective parametrization one could relate these fluctuations to the low population density of convective cloud

* Corresponding author, present address: Met Office, FitzRoy Road, Exeter, EX1 3PB, UK.
e-mail: glenn.shutts@metoffice.gov.uk

(with respect to model resolution) so that the number of clouds within a gridbox fluctuates substantially. For mountain flow drag parametrization (gravity-wave drag and 'flow-blocking' contributions) the origin of statistical fluctuation could plausibly come from nonlinearity in the flow dynamics (e.g. drag fluctuations due to eddy shedding in the low-Froude-number regime).

Apart from these early attempts to improve the skill of ensemble forecasting, considerable interest in the use of stochastic representations of atmospheric processes has developed recently and this trend seems set to continue. For instance Frederiksen and Davis (1997) developed spectral eddy viscosity and backscatter formulations for two-dimensional (2D) barotropic flow on the sphere in the context of the eddy-damped quasi-normal Markovian closure (e.g. Orszag 1970). It was shown that this backscatter formulation could provide more realistic energy spectra than conventional 'ad hoc' eddy viscosity parametrizations. Whilst their study is potentially quite relevant to the approach developed in this paper (and certainly based on a more rigorous formulation) the barotropic vorticity equation is perhaps too idealized a description of those processes involved in real atmospheric dissipation and backscatter. Furthermore, the scheme developed here includes contributions from model parametrization 'physics'.

In the context of the parametrization of deep convection in the tropical atmosphere, Lin and Neelin (2000, 2002) have experimented with different strategies to account for higher-moment fluctuations in vertical fluxes and precipitation rate. Since deep convection plays a dominant role in tropical circulation—both with respect to the mean climatology and low-frequency oscillations—it is important to establish whether the effect of these statistical fluctuations in convection is important. They found that although the near-grid-scale dynamical response of the model they used made it difficult to achieve the desired statistical behaviour, the impact of stochastic convection parametrization on low-frequency tropical wind variability was substantial.

Williams *et al.* (2004) have shown how small-amplitude stochastic perturbations representing the effects of inertia–gravity waves can influence wave number selection in a model of a rotating annulus. They directly forced the potential-vorticity field of a two-layer quasi-geostrophic model using suitably scaled random numbers, though without spatial or temporal correlations. The effect of the perturbations was only large in certain favourable regions of parameter space close to wave number transition boundaries. Their numerical simulations complement and support the findings of rotating annulus experiments in which spontaneously generated inertia–gravity waves assist wave number transition (Williams 2003).

Outside of model parametrization schemes, truncation error in the computation of advection reduces the variance in model fields. In practice, a level of horizontal diffusion is required to maintain smoothness at the grid-scale, dependent on the diffusive properties of the advection scheme in use. For instance in the semi-Lagrangian advection scheme interpolation of field values to the departure point has a net smoothing effect, with cubic interpolation behaving like bi-harmonic diffusion (McCaplin 1988). Although observational estimation of the magnitude of turbulent energy dissipation is notoriously difficult (Kennedy and Shapiro 1975; Chapman and Browning 2001) it seems likely that these model diffusive effects consume kinetic and available potential energy (APE) at an unrealistically excessive rate. For instance, horizontal diffusion and interpolation error limit the frontogenesis process in numerical weather prediction (NWP) models but are unlikely to be a satisfactory representation of the true discontinuity-limiting physical process e.g. Kelvin–Helmholtz instability.

In the context of large-eddy simulation (LES) of the turbulent boundary layer, Mason and Thomson (1992) demonstrated the positive impact of near-grid-scale

stochastic momentum forcing scaled with the local kinetic energy dissipation rate. They reasoned that the viscous drain of energy by the Smagorinsky–Lilly formulation of eddy viscosity reduces the effectiveness of poorly resolved eddies in transporting momentum to the surface. In order to match the momentum flux by larger-scale eddies, the explicitly resolved flow must sustain stronger near-surface mean shear, and the simulated flow departs significantly from the observed logarithmic variation with height. Their *stochastic backscatter* formulation excites energy at scales close to the model truncation limit, and represents a flow of energy from subgrid-scales to explicitly resolved scales. In simulations with stochastic backscatter, vertical profiles of horizontally averaged flow more nearly approximate the textbook logarithmic law.

It is argued here that the energy sink implied by numerical advection error and horizontal diffusion in NWP models is unrealistically large, and that a suitably contrived near-grid-scale stochastic forcing function could be used to inject energy back into the model in a similar manner to the stochastic backscatter approach of Mason and Thomson. However, in the NWP setting there are several additional subgrid-scale kinetic energy sources to be considered, such as that associated with the rate of working of the buoyancy force in cumulus convection.

In this paper it is shown how the computation of these kinetic energy sources in the ECMWF forecast model can be combined with a cellular automaton (CA) pattern generator to define a backscatter algorithm entitled CASBS—cellular automaton stochastic backscatter scheme. The impact of CASBS on ensemble forecasts is assessed in relation to the current operational 'stochastic physics' scheme using standard probabilistic measures of forecast skill.

The reader should be reminded at this stage of the very different rationale for model perturbations in the operational stochastic physics scheme as opposed to the backscatter scheme used here. The operational ECMWF stochastic physics scheme is a method of accounting for the underlying statistical nature of the model parametrization scheme, by allowing random fluctuations in the parametrized forcing about an assumed ensemble average that the parametrization scheme is designed to represent. The backscatter scheme addresses a missing dynamical process, i.e. the two-way exchange of kinetic energy across the model truncation boundary in wave number space, and uses the unpredictable nature of this exchange to randomly force the forecast model's vorticity field. Both techniques could be used together to perturb the ensemble member forecasts since they are both built on sound physical principles.

The outline of the paper is as follows. The physical motivation behind CASBS is described in section 2 and its implementation in the ECMWF model is outlined in section 3. In section 4 the character of the dissipation and backscatter forcing fields is examined, and the impact of CASBS on forecast skill in two sets of ten forecasts is described; concluding remarks are in section 5.

## 2. Physical basis for energy backscatter

### (*a*) *Energy backscatter estimates*

Since observational estimation of atmospheric energy dissipation rates is subject to considerable uncertainty, the task of estimating local up-scale energy transfer rates will also be prone to much error. The intensity of turbulent kinetic energy dissipation will naturally vary by orders of magnitude from place to place given its cubic dependence on velocity, and so representivity will always be a problem—even if measurement techniques were accurate. In spite of these problems, the global-mean energy dissipation rate

associated with vertical mixing can be assessed from NWP models and is probably accurate to within a factor of two. In the ECMWF model the global-mean energy dissipation rate due to parametrized vertical mixing is $\sim 2$ W m$^{-2}$. If the mean boundary-layer depth is taken to be about 1 km and air density $\sim 1$ kg m$^{-3}$ then the mean energy dissipation rate per unit mass ($\varepsilon$) is $\sim 2 \times 10^{-3}$ m$^2$s$^{-3}$. Suppose that the dissipation rate due to other local sources in the free atmosphere (e.g. gravity-wave breaking over a broad mountain range) is comparable in size. If one tenth of this is transferred up-scale rather than dissipated as heat, the associated energy backscatter rate ($\varepsilon_b \sim 2 \times 10^{-4}$ m$^2$s$^{-3}$) implies an energy tendency of about 20 m$^2$s$^{-2}$(day)$^{-1}$, which is equivalent to a local flow acceleration of $\sim 4$ or 5 m s$^{-1}$(day)$^{-1}$. This force (per unit mass) is quite small relative to a typical Coriolis force magnitude of $10^{-3}$ m s$^{-2}$ or roughly 100 m s$^{-1}$(day)$^{-1}$ (taking $f = 10^{-4}$ s$^{-1}$ and wind speed $V = 10$ m s$^{-1}$). Since the Lagrangian flow acceleration of air parcels is about one tenth of this, it is likely that the above backscatter forcing should have a tangible impact on forecast evolution, particularly in regions of intense dissipation.

Having demonstrated the plausible influence of kinetic energy backscatter on forecast model evolution, we now consider in detail the various physical and numerical sources of dissipation that are used to obtain an estimate of the total energy dissipation rate.

### (*b*) *Horizontal diffusion and interpolation error*

The inclusion of horizontal diffusion in NWP or climate models is rarely justified on physical grounds and, in any case, many types of advection scheme are inherently diffusive. Diffusion acts to maintain smooth fields at the grid-scale, preventing noise associated with frontal discontinuity formation, topographic fields and convection parametrization. Numerical advection schemes such as the semi-Lagrangian technique may be used without the need for horizontal diffusion since interpolation itself acts to smooth fields. In practice, best results are obtained with a judicious choice of horizontal diffusion that matches the inherent diffusivity of the advection scheme. This combined diffusive effect of horizontal diffusion and interpolation error on the energy will henceforth be referred to as 'numerical energy dissipation'. All other contributions to the energy dissipation arise from physical parametrization terms in the model equations. The aim of this section is to provide some support for the idea that numerical energy dissipation is excessive in NWP models.

Direct estimates of the energy dissipation due to interpolation error in the forecast model are not presently available, but some published energy diagnostics from other models help to assess the total numerical dissipation. Côte and Staniforth (1988) and Ritchie (1988) carried out 20-day integrations of the shallow-water equations with different forms of the semi-Lagrangian advection algorithm and found a 3% total energy loss over the integration period. The conservation properties of these semi-Lagrangian schemes are shown to be similar to, or somewhat better than, those in a spectral model of equivalent resolution that uses $\nabla^4$ hyperviscosity. The spectral model conserves energy in the absence of numerical smoothing, and so the hyperviscosity leads to similar energy losses as interpolation error in the semi-Lagrangian model. It will be assumed, therefore, that the energy dissipation rates found in spectral models with hyperviscosity are representative of the numerical energy dissipation rates in semi-Lagrangian models. However, the levels of dissipation found in these shallow-water model simulations are unlikely to be realistic given that the equations do not support frontogenesis and have no vertical wind shear.

The idealized baroclinic-wave life cycle experiments of Simmons and Hoskins (1978) provide some measure of the likely levels of dissipation in a NWP context. Their Fig. 4 shows a time series plot of globally averaged energy conversions and dissipation due to internal diffusion over the course of a baroclinic-wave development and its subsequent decay. Internal diffusion is represented by a $\nabla^4$ hyperviscosity term acting on vorticity, divergence and temperature; in the mature phase of the baroclinic wave this results in a peak energy dissipation rate of about 0.8 W $m^{-2}$. No surface boundary-layer parametrization was included.

MacVean (1983) looked at the effect of differing levels of scale selectivity in hyperdiffusion at different horizontal resolutions. He found that the total energy dissipation over the course of a baroclinic life cycle appears to converge to a value that represents about 45% of the total conversion of potential energy to kinetic energy as the scale selectivity is increased. As speculated by Simmons and Hoskins (1978), this suggests that the amount of energy dissipated is set by large-scale flow information in the initial state rather than the precise form of the diffusion term, provided that the baroclinic wave and associated fronts are sufficiently well resolved. The total energy dissipation in MacVean's simulations over the whole baroclinic life cycle amounts to about $2 \times 10^5$ J $m^{-2}$ which is equivalent to $\sim$0.2 W $m^{-2}$ over a time-scale of 10 days (typical of the active phase) . A visual estimate of the mean dissipation rate in the Simmons/Hoskins life cycle experiment (based on their Fig. 4) suggests a similar value.

Stephenson (1994) examined the sensitivity of a spectral general-circulation model to changes in the hyperdiffusivity and found a large impact on certain energy conversion terms. He also showed an energy box diagram derived from ECMWF analyses for the winter of 1991/92 in which the implied net dissipation of kinetic energy is 1.53 W $m^{-2}$. Unfortunately, the contribution of horizontal smoothing to this total dissipation value was not presented, and boundary-layer friction is likely to be the dominant contribution.

From a different viewpoint Blumen (1990) used a semi-geostrophic model of frontogenesis to examine the development of fronts in the presence of momentum diffusion. The collapse of the near-surface frontal width to zero is prevented by diffusion, and kinetic energy is dissipated in the resulting mixing zone. Energy dissipation rates as large as 50 to 250 W $m^{-2}$ are found in the model, though Blumen warns of the inherent uncertainty in the value. In spite of these huge values (nearly two orders of magnitude greater than a nominal boundary dissipation value) he estimates that the global-mean energy dissipation due to horizontal mixing in fronts is less than the global-mean boundary-layer dissipation. Blumen's model is likely to be representative of the balance of physical processes that occur in NWP model fronts where numerical diffusion limits scale collapse to a discontinuity. The convergence of the energy dissipation rate found by MacVean (1983) with increasing scale selectivity is relevant to mathematical solutions in which horizontal hyperviscosity plays a key role. However Cullen and Purser (1984) showed, in an extended Lagrangian semi-geostrophic model, that it is not necessary to invoke viscosity after the point of frontal collapse. Inviscid solutions could still be constructed but now with a discontinuity surface protruding from the boundary. Whilst one would not want to claim that such solutions are accurate models of real frontogenesis, they emphasize the possibility that frontal collapse can proceed down to very small horizontal scales (e.g. comparable with the depth of the boundary layer) without the need to invoke vigorous horizontal mixing.

Observational measurement of frontal dissipation is difficult to make, although Kennedy and Shapiro (1975) using aircraft data estimate energy dissipation rates of $\sim 2 \times 10^{-2}$ $m^{-2}s^{-3}$ (equivalent to $\sim$75 W $m^{-2}$ over the dissipating layer) in an upper front. There is, however, some doubt as to the representivity of such high values.

Chapman and Browning (2001) carried out a systematic study of the Doppler spectrum width from high-resolution radar, and estimate a spatially averaged frontal energy dissipation rate of $\sim 10^{-3}$ m$^2$s$^{-3}$, which is about 5 percent of the Kennedy and Shapiro estimate. As a mass-weighted vertical integral this corresponds to a few W m$^{-2}$, i.e. similar to a typical frictional boundary-layer dissipation rate and far smaller than Blumen's model estimate. The energy dissipation occurred in shallow-sloping layers of high-intensity turbulence embedded within the frontal zone, which is consistent with vertical mixing in zones of high shear. Horizontal mixing in regions of high lateral shear, as represented in NWP models, is not a very convincing physical model of the process that opposes frontal collapse. One could speculate that the energy dissipation rates found in Blumen's model and MacVean's sensitivity study are too high, and characteristic of an unphysical description of frontogenesis in which horizontal smoothing or mixing dominate over the familiar vertical mixing in low-Richardson-number shear layers.

In the context of stochastic backscatter we imagine that a substantial part of the kinetic energy lost through horizontal diffusion or semi-Lagrangian interpolation error is not dissipated by turbulence but effectively remains as a hidden subgrid-scale contribution. Horizontal diffusion in a forecast model is regarded as one of many processes that contribute to the subgrid-scale kinetic energy, of which a certain fraction should be 'backscattered' into the partially resolved scales of an NWP model.

### (*c*) *Mountain and gravity-wave drag*

In most current NWP models the effect of subgrid-scale orography is parametrized through a low-level-flow blocking drag force and a term describing the effect of stationary gravity waves. The force opposes the local flow and so appears in the energy equation as a sink of kinetic energy. From a numerical standpoint the dissipation of energy implied by this type of parametrization may locally be very large; in the ECMWF forecast model values as high as 200 W m$^{-2}$ are common over the mountains of the Himalayas and South American Andes. As with frontal dissipation, one might question whether or not this dissipation rate reflects real turbulent energy dissipation and conversion to heat, or whether a large fraction goes into subgrid-scale motion and then back up-scale. The drag force associated with flow past mountainous islands is associated with pressure differences across orographic features of differing scales. The small-scale features generate 3D turbulence, whereas island-scale orography generates quasi-2D eddies (the familiar von Karman vortices seen in downstream cloud formations). These quasi-2D motions in a stratified fluid are subject to Fjortoft's theorem (Fjortoft 1953) which requires that spreading of energy in wave number space is accompanied by more energy flowing up-scale than down-scale due to the enstrophy conservation constraint. Consequently it is difficult for such motions to dissipate energy, and the eddies shed from mountains may be absorbed into the larger-scale flow or coalesce with each other. Most of the 3D turbulent energy is dissipated at the molecular level as heat, and only a small fraction is available to backscatter onto the near grid-scale of NWP models.

Another part of the total mountain drag force is due to radiating internal gravity waves that transmit their drag contribution to regions remote from the mountain (e.g. the stratosphere). Subgrid-scale gravity-wave breaking generates potential-vorticity anomalies as well as 3D turbulence, and the former may contribute to an up-scale transfer of energy in the same manner as quasi-2D vortices shed from mountains. The efficiency of energy backscatter due to these mountain-related processes is not known, and it is necessary to appeal to 2D turbulence theory to make some plausible estimates.

### (*d*) *Deep convection*

Buoyancy forces in convective clouds generate kinetic energy on a range of scales that extend from the 1 km scale of boundary-layer cumulus out to the 500 km scale (or more) of mesoscale convective anvils. Most convective parametrization schemes do not explicitly address the fate of the kinetic energy released by buoyancy, focusing instead on the thermodynamic impact of a large population of subgrid-scale clouds as a function of the convective mass flux. In the context of shallow convection in boundary layers, energy in the convective circulations will dissipate as 3D turbulence, radiate as gravity waves out of the boundary layer or be converted to potential energy. From a thermodynamic viewpoint the warming that results from kinetic energy dissipation is negligible compared with that due to surface energy fluxes, and is often neglected in parametrization schemes.

Lilly (1983) put forward the view that a small fraction of the turbulence generated in convective anvils might participate in an up-scale energy cascade consistent with the observed $k^{-5/3}$ spectrum at horizontal wavelengths less than about 400 km (Nastrom and Gage 1985). He argued that only a few percent of the total energy dissipation rate would be required to account for the shallow spectral slope at small to mesoscales. Vallis *et al.* (1997) carried out simulations with a cloud-resolving model with a view to quantifying the up-scale influence of deep convection and examining the effect of background rotation. They found an energy spectrum at statistical equilibrium not dissimilar to the $k^{-5/3}$ power law, though the up-scale energy flux was rather weak implying an energy source for wavelengths between 60 and 300 km of $\sim$0.1 $\mathrm{m^2 s^{-2}}$ per day or $\sim 10^{-6}$ $\mathrm{m^2 s^{-3}}$. The character of the convection simulated by Vallis *et al.* (1997) is reminiscent of that found in cold cyclonic airstreams over the sea in winter, i.e. organized into cells and lines with about 30 to 60 km spacing.

The efficiency of up-scale energy transport is substantially greater for continental mesoscale convective systems where large amounts of mass are convected into the upper troposphere during the lifetime of the storm. Under these conditions Shutts and Gray (1994) showed that as much as 30% of the kinetic energy released may be trapped in balanced flows with distinctive potential-vorticity features. In the following section, it will be shown how the rate of export of kinetic energy to the cloud environment can be estimated in the ECMWF convective parametrization scheme (Tiedtke 1989).

## 3. Cellular automaton stochastic backscatter scheme (CASBS)

### (*a*) *Background*

The stochastic backscatter scheme of Mason and Thomson (1992) creates a pattern of near-grid-scale forcing by defining a 3D vector potential from random number triplets at each grid point, scaled with the square root of the 'energy drain', i.e. the rate of energy loss due to eddy viscosity. The components of the vector potential corresponding to each random number are smoothed with a 1–2–1 filter, and a momentum source is defined from the curl of the resulting vector field thereby ensuring a non-divergent forcing function. If the energy drain were to be spatially uniform, the smoothed field of random numbers would dictate the pattern of momentum forcing.

It was decided at a fairly early stage of this work to use a CA to generate spatially and temporally coherent patterns of forcing, following the suggestion of Palmer (1997). In his view the CA would be probabilistic to the extent that the probability of cell birth and survival would depend on the number of living nearest neighbours and some forecast model parameter. For instance, he envisaged a CA that would mimic

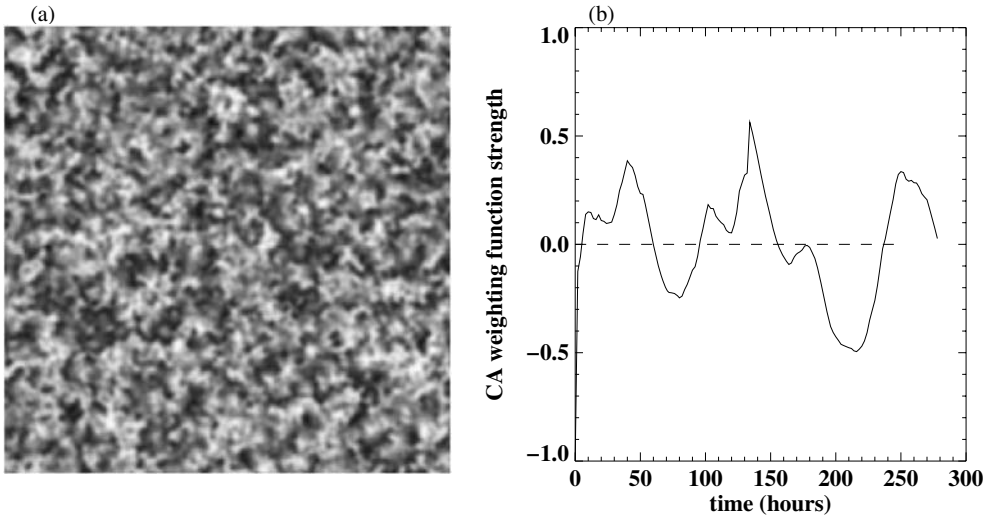


Figure 1. Examples of: (a) a field of real numbers, $\Psi$, derived from the cellular automaton (CA), values range from $-1$ (black) to $+2$ (white) and their domain mean is zero; (b) a time series of $\Psi$ at a point.

convective cloud clustering on a scale that would be functionally dependent on the local value of convective available potential energy (APE). In contrast, the CA used here is independent of the forecast model, i.e. it is simply a pattern generator. It does however have the potential to be coupled to the model fields, though at this stage there is some merit in minimizing complexity wherever possible.

A description of the CA pattern generator used here can be found in Shutts (2004). It provides a field of real numbers, $\Psi$, whose domain mean is zero and whose range is typically $-1$ to about $+2$. The patterns, an example of which is shown in Fig. 1(a), evolve as the dark 'wavefronts' propagate into the white areas. A time series of $\Psi$ at a single point (Fig. 1(b)) shows variability on a period of $\sim$3 days, and a fair degree of regularity resulting from recurring passage of wave fronts on a time-scale related to the number of lives assigned to each cell (here set to 32) and the CA time step (2 h). At the time of writing, no attempt has been made to optimize the CA's properties with respect to impacts on EPS skill: the results should be taken as a demonstration of the concept.

Ideally it would be desirable for the backscatter scheme to introduce balanced potential-vorticity perturbations into the near-grid-scale flow to minimize the production of gravity waves. As a compromise it is expedient to introduce pure vorticity perturbations into the model flow and tolerate some geostrophic adjustment. By analogy with LES stochastic backscatter, the CA pattern (suitably scaled with the square root of the dissipation rate) is taken to be proportional to a stream-function forcing.

### (*b*) *Implementation details*

A stream-function forcing field is defined from the product of $\Psi$ and the square root of a spatially smoothed form of the total energy dissipation rate ($\widehat{D}$), which is computed by summing contributions from the processes outlined in the previous section. Because the computed energy dissipation rate is a noisy field at the near-grid-scale (reflecting the character of the physical parametrization increments) it is spectrally smoothed by

multiplying the spherical harmonic coefficients by the function $S(n)$ given by:

$$S(n) = \begin{cases} 1 & n < n_f \\ \exp\left\{-3\dfrac{n(n+1) - n_f(n_f+1)}{n_c(n_c+1) - n_f(n_f+1)}\right\} & n_f < n < n_c, \\ 0 & n > n_c \end{cases} \tag{1}$$

where a filter value $n_f = 30$ and a cut-off value $n_c = 40$ are used here. The smoothing of the dissipation-rate field may be regarded as a crude device for obtaining a local ensemble-average dissipation-rate field. At an obvious practical level, the computed dissipation rate in a region of active convection like the tropical west Pacific looks quite spotty and, whilst a part of this could be real (e.g. linked to island convection), a substantial fraction will be associated with numerical noise. The backscatter forcing function is defined by the following equation for the stream-function forcing function $F_\psi$:

$$F_\psi = \tfrac{1}{2}\alpha \cdot \Delta s \Psi(\lambda, \phi)\sqrt{\Delta\tau \cdot \widehat{D}}/\Delta\tau, \tag{2}$$

where $\Delta\tau$ is the time step between successive CA states, $\Delta s$ is a nominal CA gridlength and $\alpha$ is a non-dimensional parameter that determines the backscatter fraction, i.e. the fraction of the computed energy dissipation rate that is forced back into the near-grid-scales. Note that the product $\Delta\tau \cdot \widehat{D}$ represents the increase in subgrid-scale kinetic energy during a single CA time step, and so its square root is a characteristic subgrid wind speed fluctuation. The unsmoothed dissipation rate, $D$, is made up of contributions from numerical sources ($D_N$), mountain gravity-wave drag ($D_{GW}$) and deep convection ($D_C$). Since horizontal diffusion is applied in spectral space, $D_N$ is computed by transforming the spectral vorticity and divergence increments into increments of the wind components $u$ and $v$ on the reduced Gaussian grid of the forecast model, *and* multiplying by their corresponding local wind components. Summing these component contributions gives the kinetic energy change in the resolved flow, which may be positive or negative locally.

Horizontal diffusion and smoothing due to interpolation also affect the temperature field.

The corresponding rate of loss of APE is crudely estimated using a quasi-geostrophic definition, i.e.

$$APE = \frac{g}{2B_0(z)}\left(\frac{T'}{T_0}\right)^2, \tag{3}$$

where $T'$ is the departure of the temperature from a height-dependent basic-state value $T_0(z)$ and $B_0(z)$ is the static stability. For convenience it is effectively assumed that:

$$B_0(z) = B_0(0)\left(\frac{T_0(0)}{T_0(z)}\right)^2,$$

so that (3) becomes:

$$APE = \frac{g}{2B_0(0)T_0(0)^2} \cdot T'^2, \tag{4}$$

with $B_0(0) = 1 \times 10^{-5}\ \mathrm{m}^{-1}$ and $T_0(0) = 300\ \mathrm{K}$.

In the forecast model, $T'$ is computed by removing spectral contributions with $n \leqslant 2$ from the spherical harmonic expansion of potential temperature. The APE tendency is then determined by multiplying the grid point temperature tendency associated

with horizontal diffusion by $gT'/(B_0(0)T_0(0)^2)$. Given the considerable uncertainty associated with the fraction of energy backscattered, the inaccuracy of this quasi-geostrophic definition of APE is not an overriding concern. The APE tendency is included in the total dissipation variable $D$, with the tacit assumption that only kinetic energy will be backscattered. Averaged over a sufficiently large area the diffusive contribution to the energy will be negative, representing a drain of energy from the resolved flow. $D_N$ is minus this value, and represents the rate of increase of subgrid-scale kinetic energy plus APE.

To account for the effects of semi-Lagrangian interpolation error, $D_N$ is multiplied by a certain factor determined from a simple off-line calculation. This involves computing the loss of kinetic energy in a poorly resolved idealized vortex resulting from the separate application of bi-harmonic diffusion and the forecast model's interpolation scheme. The dissipation rates associated with these two effects are of the same order of magnitude; if they were not, then horizontal diffusion would either be far too large and spoil the accuracy of near-grid-scale advection or be too small to be worth including. The factor three is used here (based on the offline calculations), implying that the diffusive influence of interpolation to the departure point is stronger by a factor of two than bi-harmonic diffusion itself.

$D_{GW}$ is computed within the operational forecast model by estimating the change in kinetic energy due to mountain drag alone. The implementation of gravity-wave and mountain flow-blocking drag in the ECMWF forecast model assumes that this energy is permanently lost from the flow and dissipated as heat, so a matching thermal increment is added to the temperature field. To be consistent with the transfer of kinetic energy back to the resolved scales, the thermal increment should be reduced accordingly. This effect has been overlooked here, but it is not thought that the impact will be significant.

The evaluation of $D_C$ is composed of two terms: one is associated with the work done on the resolved flow by the force associated with convective momentum transport; the other is due to the kinetic energy exported into the cloud environment by detrainment. The former term is evaluated in the same way as for gravity-wave drag. The other detrainment term is conveniently evaluated by multiplying the convective parametrization scheme's mass detrainment rate at any height by a locally diagnosed updraught kinetic energy (Tiedke 1989). This is obtained from the scheme's energy budget equation involving buoyancy production, entrainment and detrainment. Equation (2) is evaluated on all levels in grid point space, and then spectrally transformed so that the vorticity tendency can be computed by multiplying the resulting spectral coefficients by $-n(n+1)/a^2$, where $a$ is the earth's radius. Vorticity increments are then computed from the tendencies and added to the spectral vorticity amplitudes alongside the spectral horizontal diffusion increments.

The backscatter power spectrum is characterized in Fig. 2 by the squares of the spectral coefficients of stream-function and vorticity forcing, summed over all zonal wave numbers for each $n$. The stream function forcing (Fig. 2(a)) has a maximum near $n = 16$, corresponding to an effective wavelength $2\pi a/n(n+1) \sim 2500$ km, i.e. cyclone- or frontal-wave-scale. Given the rough equivalence of stream-function perturbation and geopotential-height or pressure perturbation, it can be seen that the backscatter scheme is forcing the height field on scales smaller than a typical midlatitude Rossby deformation radius (with effective wavelength ~6000 km) though not far removed from the baroclinically active scales. The spectral power in stream-function variance obviously emphasizes low wave numbers, and the power in $(du/dt)^2 + (dv/dt)^2$ is given by multiplying it by $n(n+1)$. Nevertheless, it could be argued that too much energy is being forced into the model at scales that should be well resolved.

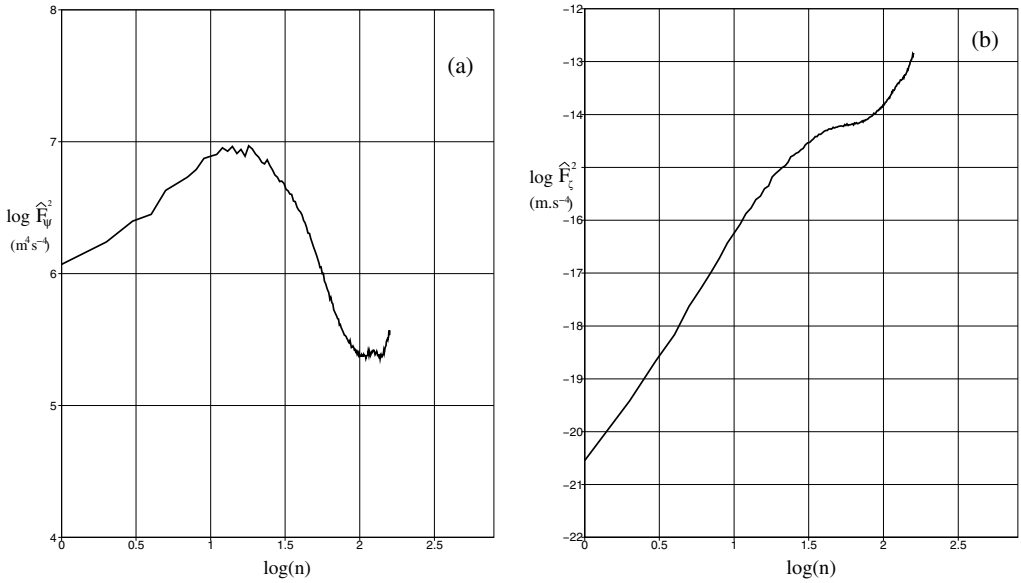


Figure 2. Spectral distributions of backscatter forcing strength as represented by: (a) $\log_{10}$(stream-function forcing variance); (b) $\log_{10}$(vorticity forcing variance).

The spectral distribution of power in the vorticity forcing function (Fig. 2(b)), obtained by multiplying the stream-function tendency power spectrum by $n^2(n+1)^2/a^4$, is a monotonically increasing function of $n$, though levelling off at $\log(n) \sim 1.7$ or $n \sim 50$, which is an effect caused by the spectral smoothing of the dissipation rate field. Its form is different from the cusp behaviour for backscatter shown in Frederiksen and Davies (1997), but the significance of this in the context of forecast model error growth is not clear.

## 4. Impact on the ECMWF forecast model

### (*a*) *Kinetic energy dissipation rate contributions*

In the absence of a theory for the backscatter ratio $\varepsilon_b/\widehat{D}$, the constant $\alpha$ in (2) should be tuned so as to maximize its positive effect on measures of EPS forecast skill, such as the rank probability skill score (RPSS). Here $\alpha$ is set to unity and $\Delta s$ is the grid length at the equator of the 2-degree grid.

For physical consistency the backscatter rate must not exceed the computed total energy dissipation rate (strictly, the energy drain rate). Before considering such matters it is instructive to look at the spatial distribution of the total dissipation rate and its decomposition into the contributions described in the last section. The total smoothed dissipation rate at T+24 h (verifying at 12 UTC on 16 October 2000) is given in Fig. 3(a). Globally averaged, this term, which represents a rate of production of subgrid-scale kinetic energy, is comparable in size with the rate of dissipation of energy in parametrized turbulent mixing (i.e. 2.87 W $m^{-2}$).

The contribution of numerical dissipation (Fig. 3(b)) is at its greatest in storm-track regions (e.g. off the east coasts of the USA and over some of the main mountainous zones such as the Andes and Himalayas) though with typical values of less than 10 W $m^{-2}$. The mountain drag contribution (Fig. 3(c)) has huge local peaks in the dissipation rate with values as high as 200 W $m^{-2}$ in the Andes.

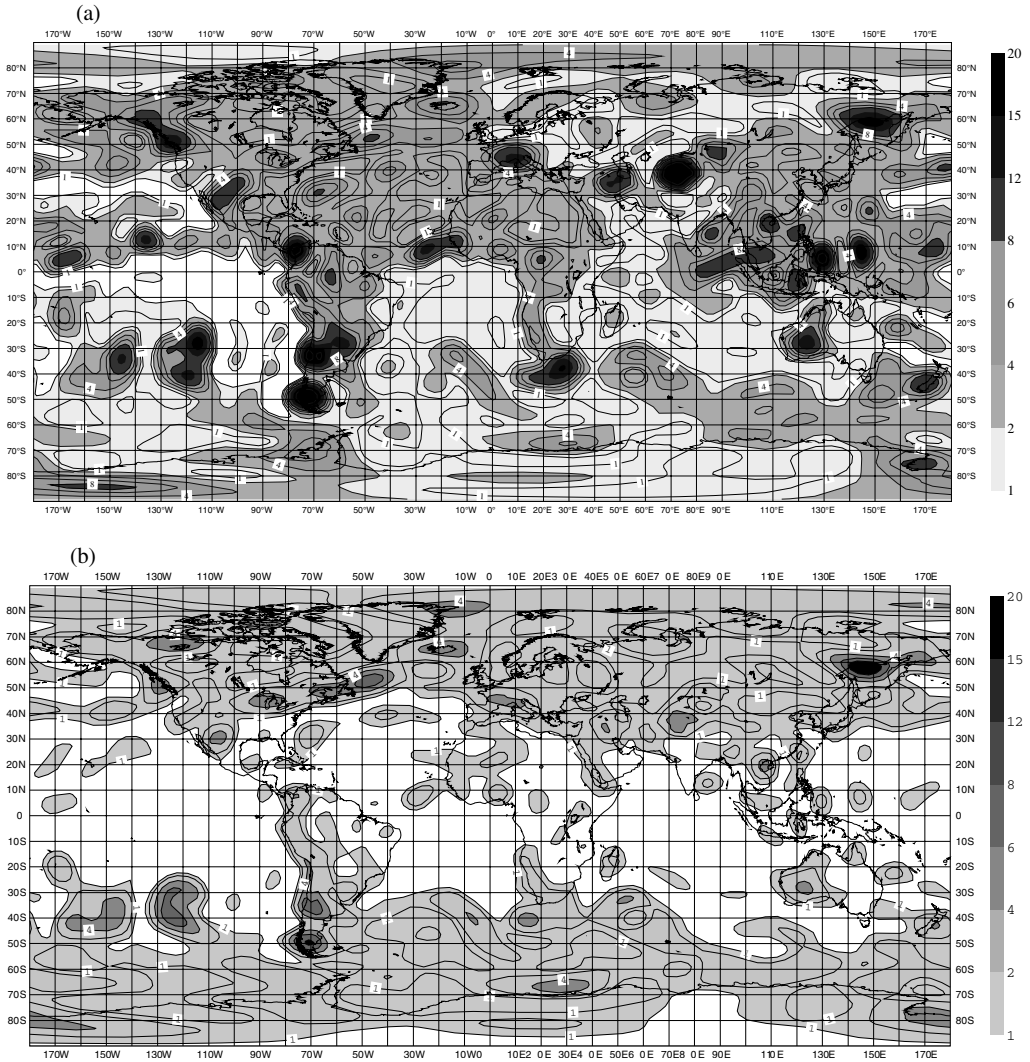


Figure 3. Kinetic energy dissipation rate contributions at T+24 h verifying at 1200 UTC 16 October 2000. (a) The total smoothed 'dissipation rate' comprising contributions from horizontal diffusion (augmented to account for semi-Lagrangian interpolation error), gravity-wave/mountain drag and deep convection; the global-mean dissipation rate is 2.87 W $m^{-2}$. (b) The smoothed numerical contribution to the total depth-integrated energy dissipation rate (W $m^{-2}$); the global mean is 1.21 W $m^{-2}$. (c) The smoothed gravity-wave and mountain drag contribution to the depth-integrated total energy dissipation rate (W $m^{-2}$); the global mean is 0.26 W $m^{-2}$. (d) The smoothed convective contribution to the depth-integrated kinetic energy source (W $m^{-2}$); the global mean is 1.27 W $m^{-2}$.

Spectral smoothing causes these to appear as circular regions extending over the sea in places. Although the energy dissipation rate due to mountain drag is locally very large, its global-mean contribution is less than 10% of the total.

Finally, the contribution of deep convection to the subgrid-scale kinetic energy is, as one would expect, concentrated in the Tropics (Fig. 3(d)). Locally the kinetic energy production rate is $\sim$20 W $m^{-2}$ and its global mean is comparable with the estimate of numerical dissipation at 1.27 W $m^{-2}$. Of course, there is a fair amount of uncertainty in the magnitude of these dissipation rates (kinetic energy production rates in the case of

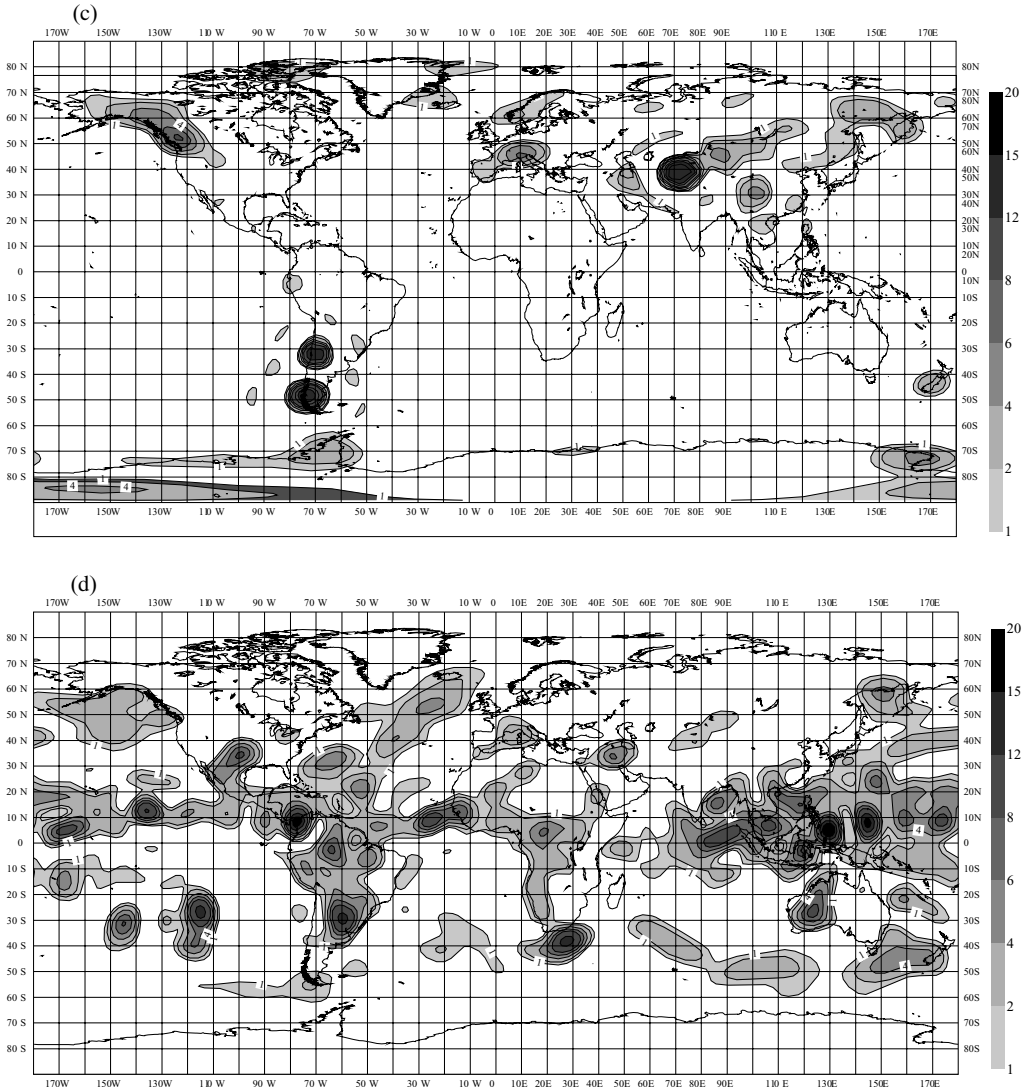


Figure 3. Continued.

convection) but since the backscatter fraction is not known this need not concern us at this stage. On the other hand, it is important to make sure that the actual rate of transfer of kinetic energy back to the resolved scales is less than the computed dissipation rate. The global rate of energy backscatter, $E_b$ is given by:

$$E_b = -\iiint \varsigma F_\psi (a/g) \cos\phi \, \mathrm{d}p \, \mathrm{d}\phi \, \mathrm{d}\lambda. \tag{5}$$

The stream-function forcing field at two model levels is shown in Figs. 4(a) and (b). At model level 47 (approximately 1.7 km above the surface) the stream-function forcing is fairly uniformly distributed over the globe, whereas at level 31 (~10.4 km) the forcing tends to dominate in the Tropics where convective mass detrainment is large. The effect of backscatter on the energy spectrum can be seen in Fig. 5, where the kinetic

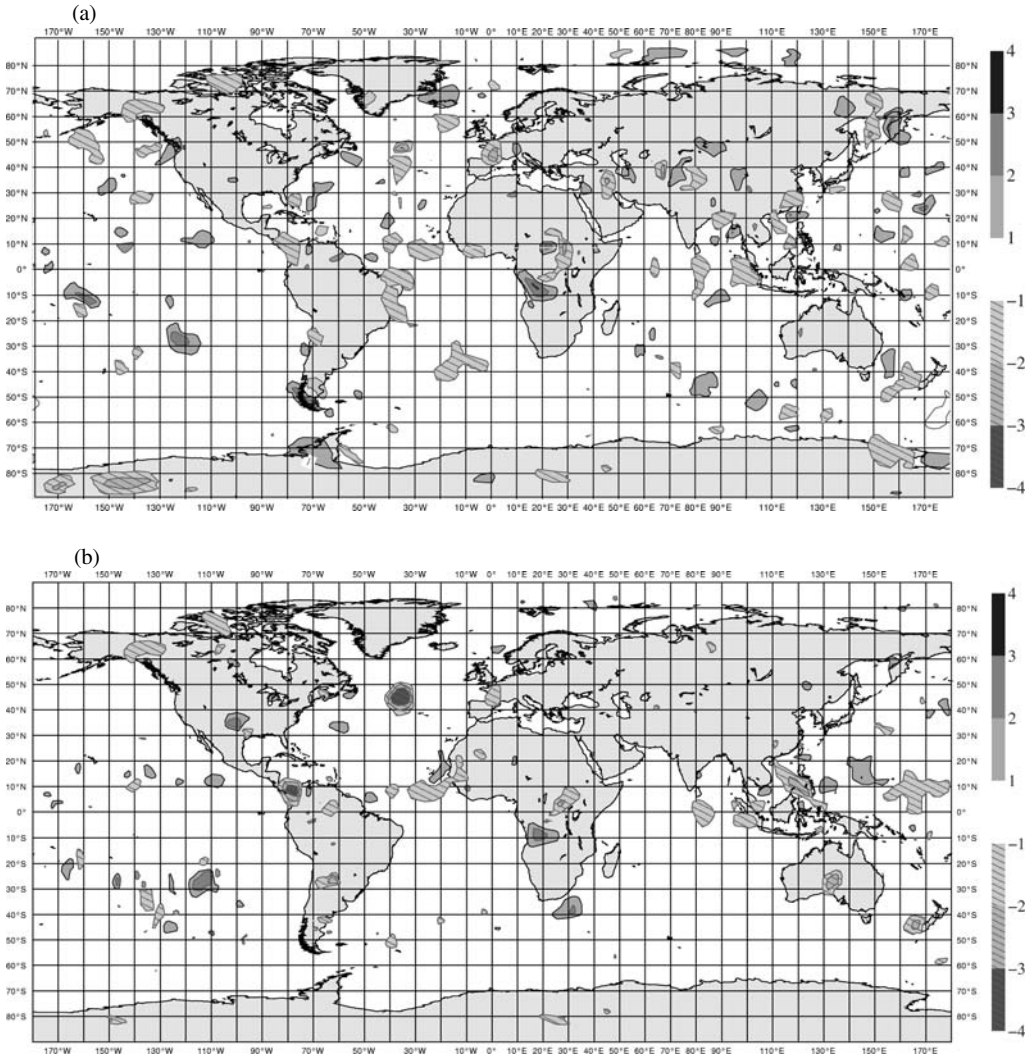


Figure 4. Stream-function forcing pattern ($F_\psi$) at two model levels: (a) level 47 (∼1.7 km), and (b) level 31 (∼10.4 km). Units are $m^2 s^{-2}$.

energy density is plotted against spherical harmonic order at T+240 h for runs with and without the stream-function forcing. The control run (without backscatter) exhibits a known deficiency of the ECMWF forecast model—the absence of a small spectral slope (approximating $k^{-5/3}$) at the smallest resolvable scales. At a spectral truncation of T159 it could be argued that there is insufficient resolution to capture the observed transition from $k^{-3}$ to $k^{-5/3}$ spectral slope. However, runs at T799 also show no sign of the $k^{-5/3}$ spectral slope (Fig. 6). With the backscatter scheme there is substantially more energy at smaller scales (Fig. 7), and it could be argued that we are compensating for a model deficiency by injecting energy at the smallest resolvable scales.

It is interesting that the energy in the divergent part of the horizontal wind *does* appear to approximately follow a $k^{-5/3}$ spectral slope. One possible interpretation of the observed $k^{-5/3}$ spectrum is that the model's divergent wind energy is suppressed at

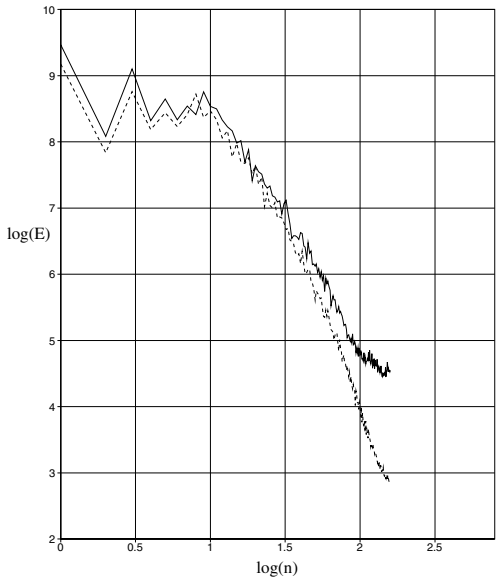


Figure 5. Kinetic energy ($E$) spectra at T+240 in the T159 control model forecast run (dashed) and with backscatter (solid). $E$ has units of $m^3s^{-2}$ and $n$ is the spherical harmonic order. The start time of the forecast is 12 UTC 15 October 2000.

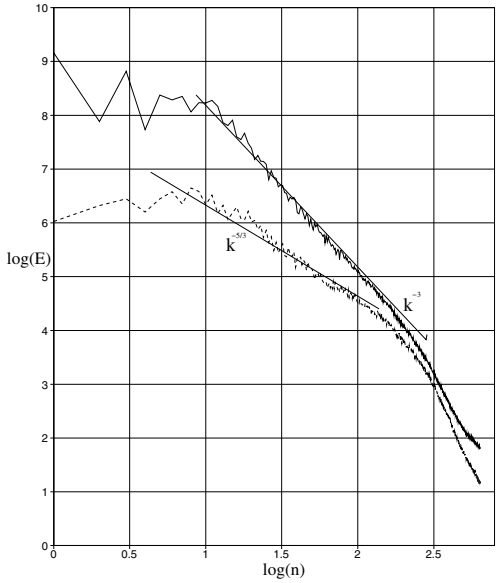


Figure 6. Energy spectra at day 10 of a model forecast with T799 resolution. The solid curve is the total kinetic energy spectrum of the horizontal wind and the dashed curve is the contribution associated with the divergent wind. The straight black lines depict the inertial sub-range, with spectral slopes of $k^{-5/3}$ and $k^{-3}$. In scales for which the spherical harmonic order $n > 200$ the energy density falls away from the corresponding constant slope line. The start time of the forecast is 12 UTC 15 October 2000.

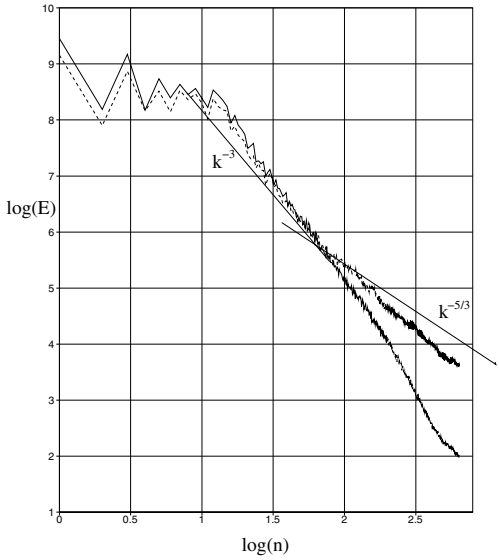


Figure 7. Energy spectra at day 5 in forecasts run at T799 resolution: with backscatter (solid curve) and without backscatter (dashed curve); $\log(E)$ is the logarithm (base 10) of the energy density and $n$ is the spherical harmonic order. The forecast start time is 12 UTC 15 October 2000.

short wavelengths, and the $k^{-5/3}$ spectral slope should extend to the smallest resolvable wavelength. This seems a compelling argument, but it is not what we are seeing in Fig. 7 since it is energy in the rotational component of the horizontal wind that dominates the spectrum for $n > 200$.

Tung and Orlando (2003) argue that the mesoscale $k^{-5/3}$ spectrum can be explained within the context of quasi-geostrophic theory (i.e. without gravity-wave contributions) as a weak energy cascade to small scales. They used a highly scale-selective hyper-viscosity ($\nabla^{20}$) that was tuned to give a very small dissipation rate (i.e. $\sim 10^{-6}$ m$^2$s$^{-3}$ which is about 0.01 W m$^{-2}$). One interpretation of the more realistic mesoscale energy spectrum in their model compared with the ECMWF forecast model is that their model better matches the real kinetic energy dissipation rate in the free troposphere. Such small dissipation rates probably cannot be achieved in the current generation of NWP models in which frontogenesis and scale collapse is more realistically described than in the quasi-geostrophic system.

### (*b*) *Effect on skill and spread in EPS experiments*

In order to quantify the effect of the CASBS scheme, sets of ten EPS forecasts have been made for the following cases:

- Initial perturbations only.
- Operational stochastic physics.
- CASBS (i.e. backscatter).

Forecasts beginning from: 12 UTC on 15 October 2000, 10, 15 and 20 November and 10, 15 and 20 December 2003, together with 9, 14 and 19 January 2004 are labelled Set A; those beginning from 12 UTC on 5, 10, 15 and 20 June, 10, 15 and 20 July, and 9, 14 and 19 August 2003 are labelled Set B. All forecasts were run for 10 days at T159 spectral truncation with 60 vertical levels and 1 h time steps. Each forecast ensemble comprises 51 members made up of one unperturbed control forecast

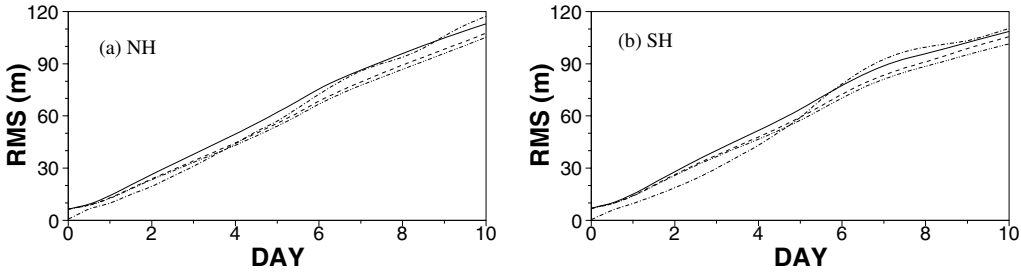


Figure 8. Spread (defined as the ensemble-average of the RMS differences between perturbed member forecasts and the control forecast for 500 hPa geopotential height) for Set A (see text) for: (a) the northern hemisphere, and (b) the southern hemisphere. The ensemble forecasts with initial perturbations only are given by the double-dot-dash curves; those with operational stochastic physics are given by the dashed curves, and those with the cellular automaton stochastic backscatter scheme (CASBS) are given by the solid curves. The dot-dash curves show the mean error of the ten control forecasts defined by the differences between forecasts and their corresponding verifying analyses.

and 50 member forecasts generated from perturbed initial conditions. Each perturbed forecast with operational stochastic physics has a different set of random numbers to use as multipliers of the model's physical parametrization tendency vector (each physical tendency also has a different random number). In the CASBS runs the CA was 'spun up' from a different random seeding of the initial state, but thereafter was not reliant upon a random number generator. In this sense the CA evolution is deterministic for each forecast member.

The impact of CASBS and operational stochastic physics is characterized by statistical properties such as the root-mean-square (RMS) spread about the control forecast and standard probabilistic measures of skill such as the Brier score, the relative operating characteristic (ROC) area and the RPSS, e.g. Jolliffe and Stephenson (2003). Attention is confined to the 500 hPa height field, $Z_{500}$, and scoring computed with respect to events with binary outcomes defined by:

$$Z_{500} - Z_{500}^{\text{clim}} > T_j, \tag{6a}$$

where $Z_{500}^{\text{clim}}$ is the climatological mean 500 hPa height field and $T_j$ is a set of positive threshold values, or:

$$Z_{500} - Z_{500}^{\text{clim}} < -T_j, \tag{6b}$$

for negative height anomaly events.

Figures 8(a) and (b) show the spread for ensemble forecast Set A over the forecast period, together with the mean error of the control runs, for the northern and southern hemispheres, respectively. In both figures the operational stochastic physics can be seen to increase the spread by a small amount though not as much as the CASBS. Good performance of the ensemble forecast system requires that the increase in spread approximately matches the growth of forecast error in the control run. Beyond day 4 or 5 backscatter is certainly increasing the spread favourably, though for shorter forecast ranges the spread is excessive. At short range (up to day 4) the spread exceeds the error of the control forecast. This will always be true at the start of the forecast because the initial state is defined to have zero error and the EPS spread at this time is meant to represent analysis error.

In general the spread and control forecast error growth is quite similar in the two hemispheres.

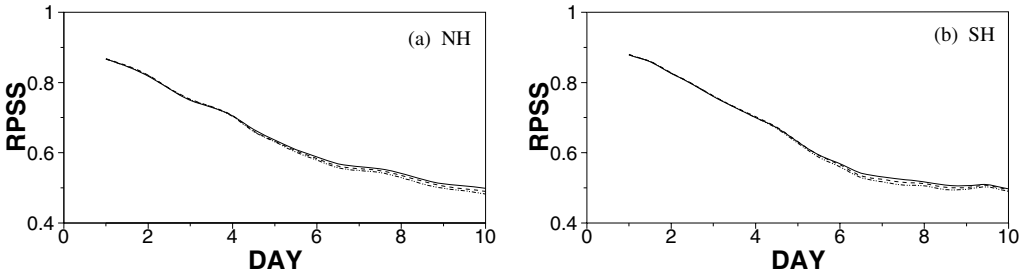


Figure 9. Rank probability skill score (RPSS) averaged over the ten Ensemble Prediction System forecasts of Set A (see text) for: (a) the northern hemisphere, and (b) the southern hemisphere. Line styles are as in Fig. 8.

Figures 9(a) and (b) show the time evolution of the RPSS based on ten thresholds for the northern and southern hemispheres, respectively. The RPSS has the advantage of effectively integrating the Brier score over many event thresholds, and so reduces the amount of information required to assess skill (as does integrating over hemispheres). The separation between the curves is not large, but it is believed that the results are statistically significant because the same ordering of skill was seen in RPSS for subsets of the ten EPS forecasts used here. Also, convergence of the RPSS curves to their form in Fig. 9 was evident as the number of EPS forecasts used was increased beyond three (i.e. when over 150 member forecasts were used). In Fig. 9(a) after day 4 it is clear that the CASBS runs have somewhat higher skill than those of the operational stochastic physics, although the differences made by either scheme are not large. In the southern hemisphere, skill improvement in the CASBS runs appears after day 6. On a cautionary note, one must assume that wobbles in the curves are a sign that the sample size is still too small. The relative spacing of dips in the curves between days 6 and 9 of Fig. 9(b) may not therefore be representative. The small overall improvements of skill later in the forecast probably follow from a better match between spread and control forecast error using CASBS (Fig. 8). The over-forecasting of spread before day 4 makes a small negative impact in skill although this is barely visible in Fig. 9(a).

Another popular analysis tool for evaluating the skill of a forecasting system is the ROC, which is a graph of hit-rate versus false-alarm-rate plotted for a range of different decision thresholds (Jolliffe and Stephenson 2003). Both hit-rate and false-alarm-rate are defined on the range 0 to 1, and the area under the curve (the ROC area) is a measure of skill with 1 being the maximum and $1/2$ corresponding to zero skill. Figures 10(a)–(e) show global ROC area plots (for Set A) versus forecast time for different 'events' of the form given by inequalities (6a) and (6b). In most cases during the first 6 days of the forecast CASBS gives a small but consistent improvement in the ROC area over the operational stochastic physics and initial-perturbations-only forecasts. Thereafter the performance of the CASBS forecasts is at least competitive with the stochastic physics scheme, and does very well indeed for $Z_{500} - Z_{500}^{\mathrm{clim}} > 100$ m which might be regarded as a test for blocking flow regimes at certain geographical locations like the European sector. Only the case $Z_{500} - Z_{500}^{\mathrm{clim}} < -25$ m has lower skill than the stochastic physics runs (and also the case $T_j = 0$ which is not shown here).

The RPSSs for northern and southern hemispheres in forecast Set B (ten forecasts from June, July and August cases) are shown in Figs. 11(a) and (b). The impact of backscatter in the northern hemisphere is less good, particularly in the first 4 days where skill is degraded with respect to the initial-perturbations-only forecast. Nevertheless the southern hemisphere RPSS shows some superiority over the operational stochastic

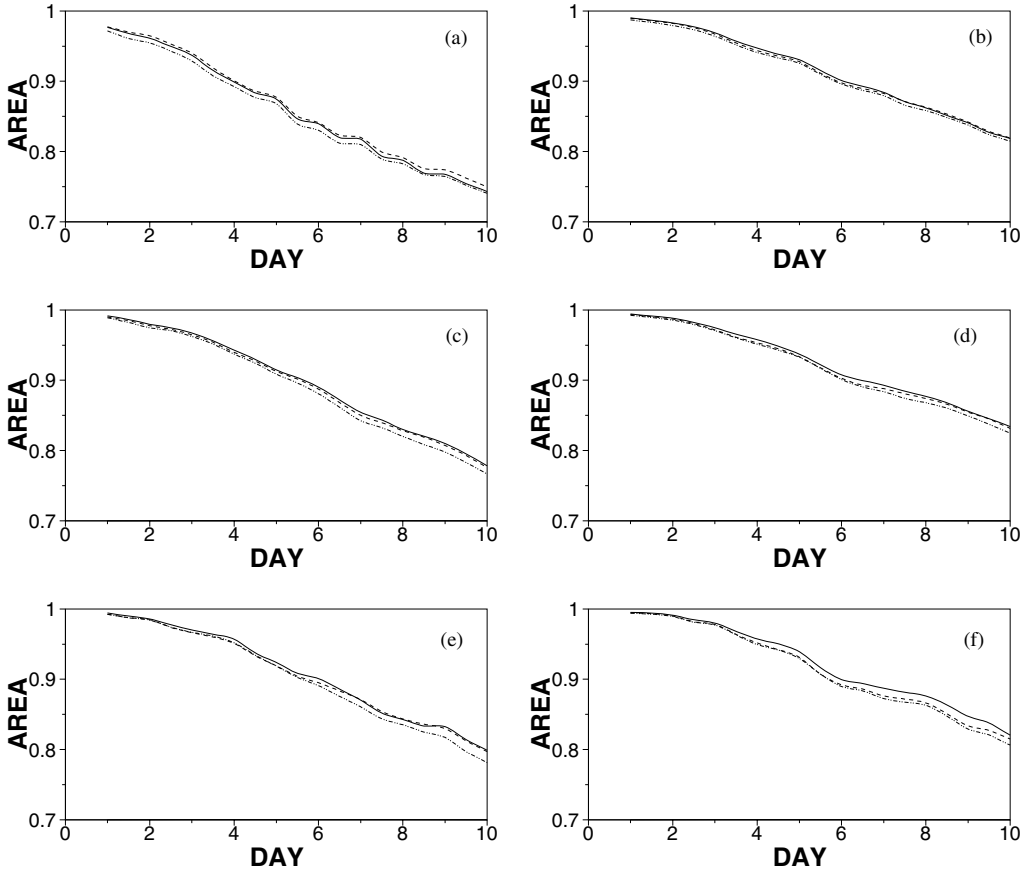


Figure 10. Mean over the ten forecasts comprising Set A (see text) of the global relative operating characteristic (ROC) area defined for six event thresholds involving the 500 hPa geopotential height ($Z_{500}$) field anomaly: (a) $Z_{500} - Z_{500}^{\text{clim}} < -25$ m; (b) $Z_{500} - Z_{500}^{\text{clim}}$ m; (c) $Z_{500} - Z_{500}^{\text{clim}} < -50$ m; (d) $Z_{500} - Z_{500}^{\text{clim}} < 50$ m; (e) $Z_{500} - Z_{500}^{\text{clim}} < -100$ m; and (f) $Z_{500} - Z_{500}^{\text{clim}} < 100$ m. The plotted curves are for the cellular automaton stochastic backscatter scheme (CASBS; solid), stochastic physics (dashed) and initial perturbations only (dotted).

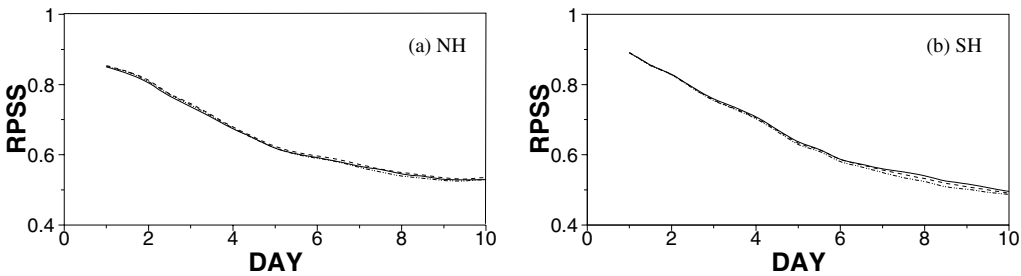


Figure 11. Rank probability skill scores (RPSS) averaged over ten Ensemble Prediction System forecasts of Set B (see text) for: (a) the northern hemisphere, (b) the southern hemisphere (line styles as in Fig. 10).

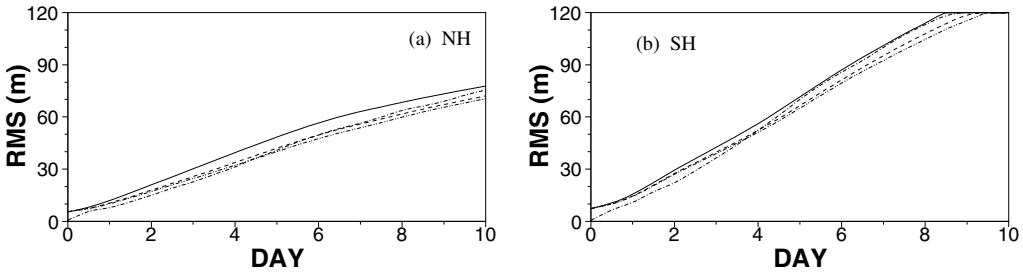


Figure 12. Ensemble Prediction System spread (as in Fig. 8) except for forecast Set B.

physics runs—similar to the skill of the Set A forecasts. Currently the reason for the degradation of the northern hemisphere summer forecasts is not known, but it may be related to excessive tropical cyclone formation. It is probably significant that the northern hemisphere summer has the weakest zonal circulation out of the four combinations of hemisphere and season, which may imply that backscatter forcing is then too strong relative to the flow strength.

The RMS forecast member spread, plotted for each hemisphere in Fig. 12, shows how the match of EPS spread to the control forecast error growth relates to skill. In the northern hemisphere the CASBS provides much more additional spread than operational stochastic physics, and this causes the spread to significantly exceed the control forecast error. In fact in these forecasts there does not seem to be a requirement for any additional EPS forecast spread beyond what is obtained from the initial perturbations. In the southern hemisphere a very good match between EPS spread and control forecast error is obtained after day 4, consistent with the good RPSS seen after day 6.

The global ROC area for Set B is shown in Fig. 13 for the same decision thresholds as for Set A in Fig. 10. Overall the performance of the CASBS relative to the operational stochastic physics scheme is quite similar to that found in Set A, with positive geopotential height anomaly events scoring much better than negative. These global-mean scores hide the poor performance in the northern hemisphere as can be seen in Fig. 14 which gives ROC area for the event $Z_{500} - Z_{500}^{\mathrm{clim}} > -100$ m. After day 4 the ROC score falls below that for the initial-perturbations-only runs, indicating a problem with over-forecasting cyclone strength.

It is also interesting to note how consistent the operational stochastic physics is in providing small improvements to the ROC area at all forecast times.

To get some idea of the sensitivity of the spread to changes in the tuneable parameter $\alpha$, which controls the stochastic forcing strength, three sets of forecasts (from the initial dates defining Set B) have been carried out using $\alpha = 0.75$, 1.0 and 1.3 (Fig. 15). Values of $\alpha$ larger than 1.3 are found to have a detrimental impact on EPS skill. The increase in spread between $\alpha = 0.75$ and $\alpha = 1.0$ is smaller than the increase between $\alpha = 1.0$ and $\alpha = 1.3$, suggesting a nonlinear dependence of spread on backscatter forcing.

## 5. Conclusions

A physical argument has been put forward for the introduction of kinetic energy sources terms into NWP models that counteract the numerical and parametrized energy drain occurring in the near-grid-scale. In this respect the approach taken here has similar motivation to energy backscatter used in LES of boundary-layer turbulence.

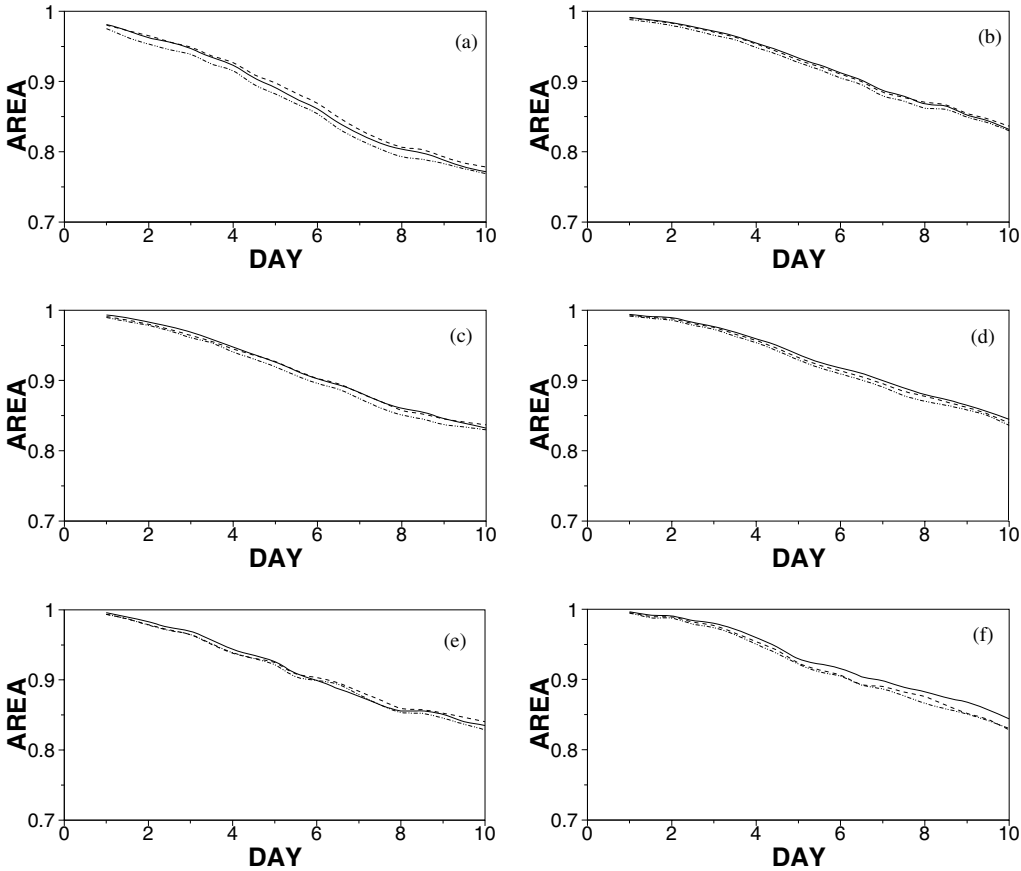


Figure 13. As Fig. 10 but for the ten forecasts comprising Set B.

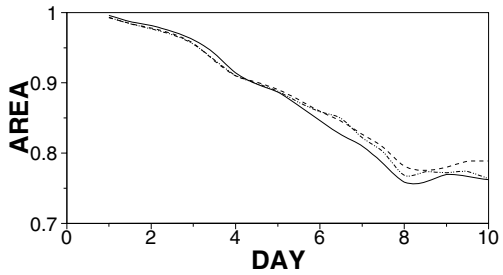


Figure 14. Relative operating characteristic (ROC) area based on $Z_{500} - Z_{500}^{\text{clim}} < -100$ m for the northern hemisphere forecasts in Set B (see text) forecasts.

In addition to offsetting the energy drain, a contribution to the net kinetic energy source is also assumed to arise from deep convection wherein a certain fraction of the kinetic energy released by buoyancy forces is assumed to be injected back onto the partially resolved scales of a forecast model. The kinetic energy contributions from these distinct numerical and physical sources are summed as a parameter called the 'total dissipation rate'.

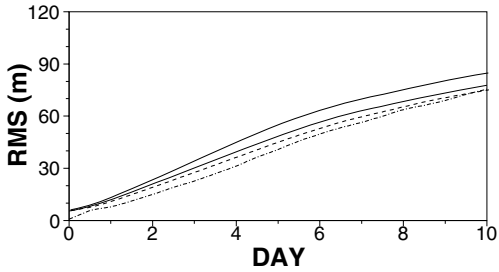


Figure 15. Ensemble Prediction System spread variation (as defined in Fig. 8) in forecast Set B (see text) for different choices of tuneable parameter $\alpha$: thick solid line, $\alpha = 1.3$; thin solid line, $\alpha = 1.0$; dashed line, $\alpha = 0.75$. The dot-dashed line is the mean error of the control forecasts (as in Fig. 12(a)).

A numerical implementation of these ideas has been developed and tested in the ECMWF forecast model energy. Kinetic energy is backscattered by introducing vorticity perturbations into the flow with a magnitude proportional to the square-root of the total dissipation rate. The spatial form of the vorticity perturbations is derived in part from a CA that crudely represents the spatial and temporal correlations of the atmospheric mesoscale. The CA is an experimental aspect of the scheme which could provide the basis for a more intelligent two-way coupled approach in which the spatial-scale of the patterns could be functionally related to the model flow. In the form used here the CA is nothing more than an exotic pattern generator, and no justification for its superiority to any other algorithm (e.g. smoothed random number fields) has been given. Further investigation into its properties and indeed other forms of CA would be desirable, particularly in a more idealized modelling context.

The CASBS is an effective means of generating EPS spread associated with model error. In the cases shown here, where the member spread about the control matches the error of the control (unperturbed) forecast, the skill of the EPS forecast is good. Because the operational stochastic physics scheme only generates a small amount of additional spread, its impact on skill is small but consistently positive. The CASBS has been tuned to provide a larger spread and these first results look encouraging, although its impact on 500 hPa skill is more sensitive to the event being forecast than the operational stochastic physics scheme. For the backscatter ratio used here ($\sim$25%) the global RPSS is somewhat better using the CASBS than the operational scheme—except for the northern hemisphere summer where the spread generated is excessive.

On a practical level, one should note that the computational demands of testing variants of the scheme is high given the large number of forecasts required for statistical reliability. It is hoped that further refinements of the CASBS will lead to more consistent and robust performance. Outstanding issues to address include: the vertical structure of the stream-function forcing; the relative contribution of the different dissipation terms; and the statistical properties of the CA. Separate process studies (e.g. with cloud-resolving models) will help to calibrate the energy backscatter ratios and provide statistical information relating to the desired spatial and temporal correlation of the stream-function forcing.

## ACKNOWLEDGEMENTS

I thank Peter Bechtold and Martin Leutbecher for considerable technical assistance during the course of this work, as well as Anton Beljaars, Roy Kershaw, Peter Janssen,

Martin Miller and Tim Palmer for many useful discussions. In particular, Peter Janssen alerted me to the deficiencies of the ECMWF model energy spectrum.

## REFERENCES


Blumen, W. 1990 A semi-geostrophic Eady-wave frontal model incorporating momentum diffusion. Part II: Kinetic energy and enstrophy dissipation. *J. Atmos. Sci.*, **47,** 2903–2908

Buizza, R., Miller, M. and Palmer, T. N. 1999 Stochastic representation of model uncertainty in the ECMWF Ensemble Prediction System. *Q. J. R. Meteorol. Soc.*, **125,** 2887–2908

Chapman, D. and Browning, K. A. 2001 Measurements of dissipation rate in frontal zones. *Q. J. R. Meteorol. Soc.*, **127,** 1939–1959

Côte, J. and Staniforth, A. 1988 A two-time-level semi-Lagrangian semi-implicit scheme for spectral models. *Mon. Weather Rev.*, **116,** 2003–2012

Cullen, M. J. P. and Purser, R. J. 1984 An extended theory of semi-geostrophic frontogenesis. *J. Atmos. Sci.*, **41,** 1477–1497

Fjortoft, R. 1953 On the changes in the spectral distribution of kinetic energy for a two-dimensional non-divergent flow. *Tellus*, **5,** 225

Frederiken, J. S. and Davis, A. G. 1997 Eddy viscosity and stochastic backscatter parameterizations on the sphere for atmospheric circulation models. *J. Atmos. Sci.*, **54,** 2475–2492

Jolliffe, I. T. and Stephenson, D. B. (Eds.) 2003 *Forecast verification: A practitioner's guide in atmospheric science*. John Wiley and Sons Ltd, Chichester, UK

Kennedy, P. J. and Shapiro, M. A. 1975 The energy budget in a clear air turbulence zone as observed by aircraft. *Mon. Weather Rev.*, **103,** 650–654

Lilly, D. K. 1983 Stratified turbulence and the mesoscale variability of the atmosphere. *J. Atmos. Sci.*, **40,** 749–761

Lin, J. W.-B. and Neelin, J. D. 2000 Influence of a stochastic moist convective parametrization on tropical climate variability. *Geophys. Res. Lett.*, **27,** 3691–3694

2002 Considerations for stochastic convective parametrization. *J. Atmos. Sci.*, **59,** 959–975

McCaplin, J. D. 1988 A quantitative analysis of the dissipation inherent in semi-Lagrangian advection. *Mon. Weather Rev.*, **116,** 2330–2336

MacVean, M. 1983 The effects of horizontal diffusion on baroclinic development in a spectral model. *Q. J. R. Meteorol. Soc.*, **109,** 771–783

Mason, P. J. and Thomson, D. J. 1992 Stochastic backscatter in large-eddy simulations of boundary layers. *J. Fluid Mech.*, **242,** 51–78

Nastrom, G. D. and Gage, K. S. 1985 A climatology of atmospheric wavenumber spectra of wind and temperature observed by commercial aircraft. *J. Atmos. Sci.*, **42,** 950–960

Orszag, S. A. 1970 Analytical theories of turbulence. *J. Fluid Mech.*, **41,** 363–386

Palmer, T. N. 1997 'On parametrizing scales that are only somewhat smaller than the smallest resolved scales, with application to convection and orography'. In Workshop on new insights and approaches to convective parametrization, 4–7 November 1996. European Centre for Medium-Range Weather Forecasts, Shinfield, Reading, UK

Ritchie, H. 1988 Application of the semi-Lagrangian method to a spectral model of the shallow-water equations. *Mon. Weather Rev.*, **116,** 1587–1598

Shutts, G. J. 2004 'A stochastic kinetic energy backscatter algorithm for use in ensemble prediction systems'. ECMWF Tech. Memo. No. 449. European Centre for Medium-Range Weather Forecasts, Shinfield, Reading, UK

Shutts, G. J. and Gray, M. E. B. 1994 A numerical modelling study of the geostrophic adjustment process following deep convection. *Q. J. R. Meteorol. Soc.*, **120,** 1145–1178

Simmons, A. and Hoskins, B. J. 1978 The life cycles of some nonlinear baroclinic waves. *J. Atmos. Sci.*, **35,** 414–432

Stephenson, D. B. 1994 The impact of changing the horizontal diffusion scheme on the northern winter climatology of a general circulation model. *Q. J. R. Meteorol. Soc.*, **120,** 211–226

Tiedke, M. 1989 A comprehensive mass flux scheme for cumulus parametrization in large scale models. *Mon. Weather Rev.*, **117,** 1779–1800

Tung, K.-K. and Orlando, W. W. 2003 The $k^{-3}$ and $k^{-5/3}$ energy spectrum of atmospheric turbulence: Quasi-geostrophic two-level model simulation. *J. Atmos. Sci.*, **60,** 824–835

Vallis, G. K., Shutts, G. J. and Gray, M. E. B. 1997 Balanced mesoscale motion and stratified turbulence forced by convection. *Q. J. R. Meteorol. Soc.*, **123,** 1621–1652

Williams, P. D. 2003 'Nonlinear interactions of fast and slow modes in rotating stratified fluid flows'. PhD Thesis, Oxford University

Williams, P. D., Haine, T. W. N. and Read, P. L. 2004 Stochastic resonance in a nonlinear model of a rotating, stratified shear flow, with a simple stochastic, inertia–gravity wave parametrization. *Nonlinear Processes Geophys.*, **11,** 127–135